Tailored Magnetic Torsion Springs for Miniature Magnetic Robots

Cameron Forbrigger, Adam Schonewille, and Eric Diller

***Abstract*— Magnetic torsion springs are capable of producing unique and useful torque-displacement responses that are not possible with elastic springs. Millimeter-scale magnetically-actuated robots, which are gaining increasing interest in biomedical applications, would benefit from the use of magnetic torsion springs. However, existing magnetic torsion springs are difficult to fabricate at that scale and can only produce sinusoid-like responses. Here we show that the magnets embedded in the links of a robot for actuation purposes can also be leveraged to produce torsion spring-like behavior. This Simultaneous Magnetic Actuation and Restoring Torque (SMART) spring design can enable switching or pop-up behaviour in millimeter-scale magnetically-actuated mechanisms. A novel analytical model, validated both numerically and experimentally, is used to design constant-stiffness and nonlinear bistable SMART springs. These springs are integrated into a novel 3.5 mm diameter magnetic robot manipulator.**

I. Introduction

Magnetic fields can penetrate physical barriers to apply forces and torques wirelessly to magnetic robotic devices in small confined environments. Magnetic robots show superior precision, directionality, and control complexity compared to other small-scale actuation methods, which makes magnetic devices an attractive engineering solution to a variety of challenges in biomedical applications and in the area of small scale mechanisms more broadly [1], [2].

In addition, integrated magnets in robotic devices can be used to store energy or provide restoring forces in place of or complementing elastic springs. Energy storage is crucial for some methods of robot locomotion, and non-linear restoring torque is necessary for mimicking biological locomotion patterns [3]. Unlike elastic springs, magnetic springs experience no fatigue and very little wear, and they can easily be embedded within mechanism links [4]. Magnetic rectilinear springs have been custom-tailored to produce nonlinear force-displacement relationships for specific actuation methods [4], [5]. Variable stiffness magnetic torsion springs have been designed for human-scale robots and mechanisms [6], [7], [8], [9] and for energy storage in centimeter-scale capsule robots [10], [11]. However, all of these previous magnetic torsion spring designs could only produce sinusoid-like torque-deflection responses, and some designs lacked magnetic actuation capabilities due to their symmetric magnet placement [6], [8], [9]. Furthermore, many of these multiple-magnet designs become increasingly difficult to manufacture on smaller scales.

Magnetic interaction scales powerfully with decreasing distance between magnets, so magnetic springs are well-suited to small-scale robots. One such application is millimeter-scale magnetic robot manipulators for tasks in confined environments. Such robots have been developed previously with elastic compliant joints composed of thin Nitinol wires [12], [13]. The restoring torque provided by the elastic joints allow the gripping and wrist actuation to be decoupled and controlled independently. However, these compliant joints have some disadvantages: notably, parasitic motion (buckling) [14] makes it difficult to predict the motion of the manipulators or apply directed forces, and they are limited to a single stable position, which can limit the available gripping or prying strength. Rigid pin joints could solve the buckling problem, but they do not provide the restoring torques that are critical to the control of the robot. Magnetically-actuated robots already have embedded magnets in their links for actuation purposes; we propose that the position and orientation of these magnets can be tailored to produce unique torque-displacement relationships that cannot be achieved by previous magnetic spring designs.

This work presents the Simultaneous Magnetic Actuation and Restoring Torque (SMART) spring design, which allows highly customizable torque-deflection responses for small-scale ($\leq$ 5 mm diameter) magnetically-actuated mechanisms. Here we show how simple two-magnet systems embedded in the mechanism links can produce unique and useful torque-displacement relationships in a compact assembly by integrating these springs into the design of a novel magnetic robot pictured in Fig. 1. In addition, we show that a simple point dipole model can model the behavior of SMART springs with sufficient accuracy to allow rapid design exploration and iteration without relying on more computationally-heavy finite element methods.

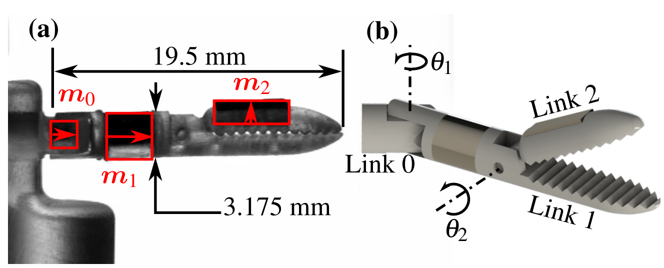

Fig. 1. **(a)** Photograph of the robot designed with magnetic torsion springs showing the locations and magnetization of the integrated magnets. **(b)** Render of the robot CAD model showing its degrees of freedom.

This work was supported in part by the Natural Sciences and Engineering Research Council of Canada through the Discovery Grant Program 2014-04703 and in part by the Canadian Institutes for Health Research under Grant CPG-158271. (*Corresponding author: Cameron Forbrigger.*)

Department of Mechanical and Industrial Engineering, University of Toronto, 5 King's College Rd, Toronto, ON M5S 3G8 cameron.forbrigger@mail.utoronto.ca

II. Analytical Model

This model will define the geometry of SMART springs, enable the prediction of their behaviour, and give insights into how their performance scales with their size. The model is valid for any mechanism (serial or parallel) with revolute joints and a single embedded magnet in each link. It assumes that magnetic interactions between non-adjacent links are negligible. In addition, the analytical model was formulated using the point dipole assumption, which assumes that a volume of magnetic material V with a uniform magnetization M can be represented by a vector quantity $\boldsymbol{m}$ with magnitude $m = MV$ located at the center of volume of the material, which simplifies the equations for magnetic fields, forces, and torques. The point dipole assumption is valid when the dimensions of magnetic objects are relatively small compared to the distances between the magnetic objects [15]. This assumption may not be valid for some designs, but it simplifies the geometry sufficiently to allow for rapid exploration of the design space before refinement of the SMART spring design with finite element models.

A. Design Parameters of a SMART Spring

The first step in developing an analytical model is to develop a consistent representation for the geometry of the SMART spring. Consider a serial mechanism with three links, each connected with revolute joints, with the first link (link 0) connected to ground as shown in Fig. 2(a). Magnetic material in each link causes intermagnetic forces and torques acting between the links that will vary with the joint angles θ_1 and θ_2. Fig. 2(b) depicts a simplified geometry used to formulate the analytical model of the SMART spring that accounts for magnetic interaction between two adjacent links A and B. In this model, a right-handed spring coordinate system $\left[\hat{\boldsymbol{i}}_A,\ \hat{\boldsymbol{j}}_A,\ \hat{\boldsymbol{k}}_A\right]$ is defined such that $\hat{\boldsymbol{k}}_A$ lies along the rotational axis of the joint and the position of the magnetic point dipole $\boldsymbol{m}_A$ lies along $\hat{\boldsymbol{i}}_A$. The spring deflection γ is defined as the angle between the position vectors of the magnets. The spring coordinate system is defined such that the conversion from the joint angle of the i^{th} joint θ_i to its spring deflection γ_i is simply $\theta_i = \gamma_i + \beta_i$, where β_i is some constant angular offset.

The positions of the point dipoles are defined as follows:

$$\boldsymbol{r}_A = r_A \begin{bmatrix} 1 & 0 & 0 \end{bmatrix}^{\mathsf{T}} , \tag{1}$$

$$\boldsymbol{r}_B = r_B \begin{bmatrix} \cos\gamma & \sin\gamma & 0 \end{bmatrix}^{\mathsf{T}} . \tag{2}$$

Where r_A and r_B are the radial distances from the point dipoles to the rotational axis of the joint. The point dipole vectors are defined as follows:

$$\boldsymbol{m}_A = m_A \begin{bmatrix} \cos(\varphi_A) & \sin(\varphi_A) & 0 \end{bmatrix}^{\mathsf{T}} , \tag{3}$$

$$\boldsymbol{m}_B = m_B \begin{bmatrix} \cos(\gamma + \varphi_B) & \sin(\gamma + \varphi_B) & 0 \end{bmatrix}^{\mathsf{T}} . \tag{4}$$

where φ_A and φ_B describe the orientation of the dipoles relative to the link to which they are fixed, and m_A and m_B represent the dipole magnitudes.

B. Behavior of a SMART Spring

The design criteria for a torsion spring can be specified in terms of its restoring torque τ_z or stiffness K_γ. In this section a method for determining these properties for SMART springs is presented, and a new quantity called the magnetic sensitivity is introduced.

Analytical expressions for the magnetic force $\boldsymbol{f}_{AB}$ and torque $\boldsymbol{\tau}_{AB}$ on a magnetic dipole $\boldsymbol{m}_B$ due to another magnetic dipole $\boldsymbol{m}_A$ are readily available elsewhere [15] but are repeated here for completeness:

$$\boldsymbol{\tau}_{AB} = \frac{\mu_0 m_A m_B}{4\pi \|\boldsymbol{r}_{AB}\|^3} \hat{\boldsymbol{m}}_B \times \left(3 \hat{\boldsymbol{r}}_{AB} \hat{\boldsymbol{r}}_{AB}^{\mathsf{T}} - \mathbb{I}_3\right) \hat{\boldsymbol{m}}_A , \tag{5}$$

$$\begin{aligned} \boldsymbol{f}_{AB} = \frac{3\mu_0 m_A m_B}{4\pi \|\boldsymbol{r}_{AB}\|^4} \Big(&(\hat{\boldsymbol{r}}_{AB}^{\mathsf{T}} \hat{\boldsymbol{m}}_A)\, \hat{\boldsymbol{m}}_B + (\hat{\boldsymbol{r}}_{AB}^{\mathsf{T}} \hat{\boldsymbol{m}}_B)\, \hat{\boldsymbol{m}}_A \\ &+ \big(\hat{\boldsymbol{m}}_A^{\mathsf{T}} \hat{\boldsymbol{m}}_B - 5\, (\hat{\boldsymbol{r}}_{AB}^{\mathsf{T}} \hat{\boldsymbol{m}}_A)\, (\hat{\boldsymbol{r}}_{AB}^{\mathsf{T}} \hat{\boldsymbol{m}}_B)\big) \hat{\boldsymbol{r}}_{AB} \Big) , \end{aligned} \tag{6}$$

where μ_0 is the permeability of free space, $\boldsymbol{r}_{AB} = \boldsymbol{r}_B - \boldsymbol{r}_A$, $\times$ denotes the vector cross product, $\|\boldsymbol{a}\|$ denotes the magnitude or 2-norm of the vector $\boldsymbol{a}$, and $\hat{\boldsymbol{a}} = \boldsymbol{a}/\|\boldsymbol{a}\|$ denotes a unit vector in the direction of $\boldsymbol{a}$.

The scalar torque component on link B about the rotational axis $\hat{\boldsymbol{k}}_A$ due to the magnetic force and torque acting on $\boldsymbol{m}_B$ can be determined directly from (5) and (6):

$$\tau_z = \hat{\boldsymbol{k}}_A^{\mathsf{T}} \left(\boldsymbol{\tau}_{AB} + \boldsymbol{r}_B \times \boldsymbol{f}_{AB}\right) . \tag{7}$$

The angular stiffness K_γ (N·m/rad) can found from the derivative of τ_z with respect to γ,

$$K_\gamma = -\frac{\partial \tau_z}{\partial \gamma} = \frac{\partial^2 U}{\partial \gamma^2} . \tag{8}$$

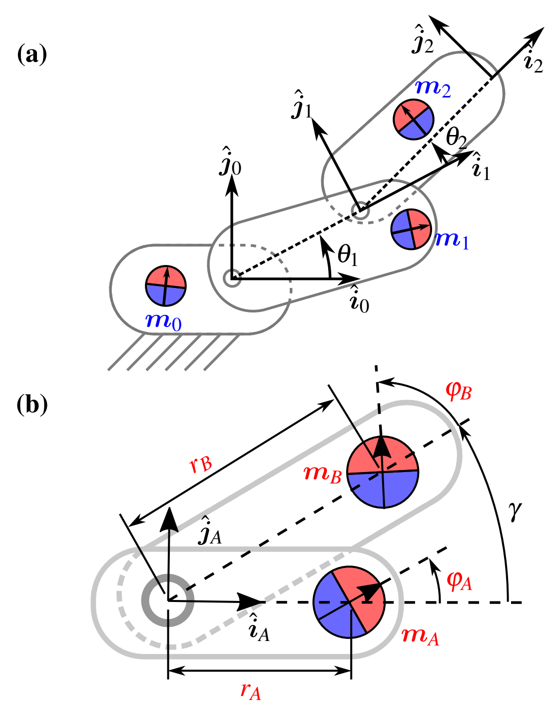

Fig. 2. (a) A magnetic serial mechanism with coordinate systems according to the Denavit-Hartenberg convention. (b) Geometry of a SMART spring with the design parameters highlighted in red.

Deriving the analytical expression for this derivative may only be tractable for the simplest cases, such as when $r_A = 0$ or $r_B = 0$. In this work, K_γ was calculated numerically from the analytical values of τ_z using a central difference approximation of the derivative.

If link B is to be actuated via magnetic field, a useful property is the magnetic sensitivity S_m (rad/T), which is defined here as

$$S_m = \frac{m_B}{K_\gamma} \, . \tag{9}$$

The magnetic sensitivity describes the angular deflection of link B that results from an applied magnetic field. A higher magnetic sensitivity indicates that larger deflections can be achieved with the same magnetic field. However, if the magnetic sensitivity is too large it may be difficult to achieve accurate small deflections.

C. Dimensional Analysis and Scaling Laws

The behaviour of the SMART spring, described by τ_z or K_γ, is a function of six independent variables. From (5) - (8) it follows that

$$\tau_z = f_\tau\left(\gamma, r_B, r_A + r_B, \varphi_A, \varphi_B, \mu_0 m_A m_B\right) \, , \tag{10}$$

$$K_\gamma = f_K\left(\gamma, r_B, r_A + r_B, \varphi_A, \varphi_B, \mu_0 m_A m_B\right) \, . \tag{11}$$

Dimensional analysis using the Buckingham Pi Theorem allows these equations to be rewritten in a unitless form, such that

$$\bar{\tau}_z = \frac{(r_A + r_B)^3}{\mu_0 m_A m_B}\tau_z = \phi_\tau\left(\gamma, \bar{R}, \varphi_A, \varphi_B\right) \, , \tag{12}$$

$$\bar{K}_\gamma = \frac{(r_A + r_B)^3}{\mu_0 m_A m_B}K_z = \phi_K\left(\gamma, \bar{R}, \varphi_A, \varphi_B\right) \, , \tag{13}$$

where $\bar{\tau}_z$ and $\bar{K}_\gamma$ are the normalized torque and stiffness and $\bar{R} = r_B/(r_A + r_B)$ is the characteristic length ratio.

The dimensional analysis reveals that the shape of the torque and stiffness functions with respect to γ depends only on $\bar{R}$, φ_A, and φ_B; therefore, if a specific spring behaviour is desired, such as specific points of equilibrium or constant stiffness, it is only necessary to search over these three dimensionless parameters to find a suitable spring geometry.

Changing the geometric scale of the spring ($r_A + r_B$) or the magnitude of the dipoles ($m_A m_B$) in the spring results only in a vertical scaling of the torque and stiffness functions. Assuming constant magnetization of the magnets in the SMART spring, and given an isotropic geometric scaling factor L such that $m_A, m_B \propto L^3$ and $r_A, r_B \propto L$, it can be seen that $\tau_z, K_\gamma \propto L^3$ and $S_m \propto L^0$. Notably, the stiffness of an elastic cantilever torsion spring $K = EI/l$ also scales with L^3; therefore, elastic torsion springs and magnetic torsion springs should be similarly effective as they are scaled down.

III. SMART Spring Design Example

The goal of this design example was to create a miniature manipulator with a constant-stiffness wrist spring and a bistable gripping finger thus demonstrating the useful spring behaviours that can be accomplished by SMART springs within a small envelope. The rough shape of the gripping digits was inspired by the Intuitive Surgical 5 mm bullet nose dissector attachment for the da Vinci robot. To reduce the scope of the design process, the magnetic actuation design of the manipulator was based on a previous single-digit magnetic gripper design that used elastic spring joints ("Design B" from [13]).

A. Constraints and Criteria

The robot has two revolute joints (wrist and finger) and three magnets: $\boldsymbol{m}_0$, $\boldsymbol{m}_1$, and $\boldsymbol{m}_2$ in the base, the wrist, and the finger, respectively. The wrist magnet $\boldsymbol{m}_1$ serves as both the distal magnet $\boldsymbol{m}_B$ for the wrist spring and as the proximal magnet $\boldsymbol{m}_A$ for the finger spring.

The design is subject to several constraints. First, to prove the applicability of these magnetic springs to small scale devices, it was decided that the manipulator must fit through a 5 mm diameter hole or smaller (less than half the size of existing magnetic torsion springs). Second, the available magnetic field generation system is capable of generating field magnitudes up to 20 mT, so it must be possible to actuate both the gripper and wrist simultaneously with less than the maximum available field strength. Third, to prove the simplicity of fabricating these springs, the manipulator must be built with off-the-shelf magnetic components. Fourth, to allow for magnetic actuation according to the design from [13], the orientation of the distal wrist magnet must be $\varphi_B = 0°$ and the orientation of the distal finger magnet must be $\varphi_B \approx 90°$. Finally, in a serial mechanism of this size it would be difficult to manufacture magnetic springs with an operating deflection range on the same side of the joint ($-90° < \gamma < 90°$), so the operating deflection range of the joints is constrained to approximately $90° \leq \gamma \leq 270°$. If the joint angles θ_1 and θ_2 are defined according to the Denavit-Hartenberg convention and if the manipulator is to be as compact as possible, these ranges of the spring deflection γ result in offset angles $\beta_1 = -180°$ and $\beta_2 \approx -180°$.

Friction becomes more significant at smaller size scales; therefore, the springs should have as high a stiffness as possible to reduce steady-state positioning errors due to friction in the joints. In addition, higher manipulator applied forces (pushing and gripping) are desirable; therefore, the wrist magnet and finger magnet should have as large a magnetic moment (volume) as possible.

B. Design Process

The first step in the design process was to choose the desired shape of the torque curve for each joint; that is, to choose $\bar{R}$, φ_A, and φ_B. The wrist joint (joint 0) needed to have a stable equilibrium at $\gamma = 180°$ ($\theta_1 = 0°$) and a nearly constant stiffness so that it returns to its resting joint angle of $\theta_1 = 0°$ when the actuating magnetic field is removed. The finger joint (joint 1) needed to have an unstable equilibrium at approximately $\gamma = 240°$ ($\theta_1 \approx 60°$) so that it experiences a bistable transition between open $\theta_2 = 90°$ and closed $\theta_2 = 0°$ positions.

To choose the values of φ_A and φ_B, the points of equilibrium for a magnetic torsion spring for a given value of φ_A and φ_B were determined using the analytical model and plotted against different values of $\bar{R}$ as shown in Fig. 3(a) and (b). For the wrist joint, $\varphi_B = 0°$ was known from the constraints, but φ_A needed to be determined. After plotting the equilibrium points for many different values of φ_A, it was found that the only values that returned stable equilibrium points at $\gamma = 180°$ were $\varphi_A = 0°$ or $\varphi_A = 180°$. However, the range of stability was larger and the linearity was better for the equilibrium points with $\varphi_A = 180°$; therefore, $\varphi_A = 180°$ was selected for the wrist spring. For the finger joint, $\varphi_A = 180°$ and $\varphi_B \approx 90°$ were known from the constraints.

The range of acceptable values for $\bar{R}$ was determined from Fig. 3(a) and (b) for the wrist and finger joints respectively. For the wrist joint, $0 \leq \bar{R} \leq 0.2$ and $0.8 \leq \bar{R} \leq 1.0$ gave stable equilibrium points at $\gamma = 180°$; however, if m_B is to be as large as possible to ensure high applied forces, values of $0.8 \leq \bar{R} \leq 1.0$ would be easier to manufacture. For the finger joint, the range of acceptable values was more restrictive: approximately $0.58 \leq \bar{R} \leq 0.62$.

Selecting an exact value of $\bar{R}$ within the range of acceptable values for the wrist spring required a closer look at the stiffness behaviour in Fig. 4. A value of $\bar{R}$ near 0.95 was chosen because it had the least variation in stiffness over the operating deflection range. Further tuning resulted in a final selected value of $\bar{R} = 0.94$ for the wrist joint.

To select an exact value of $\bar{R}$ within the range of acceptable values for the finger spring, its torque-deflection behaviour was examined in Fig. 5. Higher values of $\bar{R}$ move the unstable equilibrium point lower and provide higher torque at the lower limit of the operating deflection range (closed state) while lower values of $\bar{R}$ provide higher stiffness at the unstable equilibrium point and higher torque at the upper limit of the operating deflection range (open state). A value of $\bar{R} = 0.59$ was chosen because it yielded a reasonable trade-off between higher stiffness at equilibrium and higher torque in the closed state.

The remaining three parameters $r_A + r_B$, m_A, and m_B needed to be selected to determine the magnitude of the torque, stiffness, and sensitivity for the spring. For the wrist magnet, a 3.2 mm diameter by 3.2 mm length cylindrical magnet was chosen for m_1 (m_B for the wrist and m_A for the finger) to maximize the strength of the robot while satisfying the size constraint. Choosing the magnitude of m_0 and the distance $r_A + r_B$ for the wrist spring required manual tuning to find an acceptable mean magnetic sensitivity (140 rad/T) and mean stiffness (2.1×10^{-4} N.m/rad) over the operating range. A similar manual tuning process was performed to choose the magnitude of m_2 and the distance $r_A + r_B$ for the finger joint, resulting in a magnetic sensitivity of 65 rad/T and a stiffness of 1.9×10^{-4} N.m/rad at the equilibrium point.

C. Final Selected Design Parameters

The results of the design process are shown in Table I. The values given in bold were determined directly from the design constraints. The manipulator components were fabricated using a FormLabs Form 2 Desktop SLA 3D printer with FormLabs Clear v4 resin at a resolution of 25 μm. A D11-N52 cylindrical magnet ($D = 1.6$ mm, $H = 1.6$ mm), a D22-N52 cylindrical magnet ($D = 3.2$ mm, $H = 3.2$ mm), and three B111 cubic magnets ($L = 1.6$ mm each) from K&J Magnetics were used for $\boldsymbol{m}_0$, $\boldsymbol{m}_1$, and $\boldsymbol{m}_2$ respectively. A

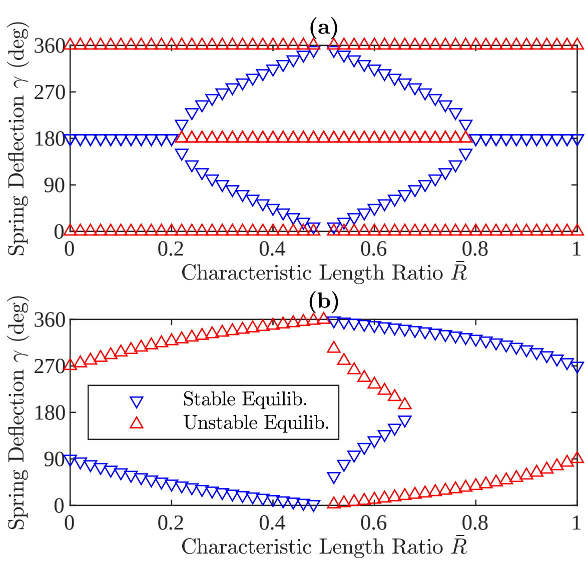

Fig. 3. Points of equilibrium for **(a)** the wrist spring $\varphi_A = 180°$ and $\varphi_B = 0°$ and **(b)** the finger spring $\varphi_A = 180°$ and $\varphi_B = 90°$.

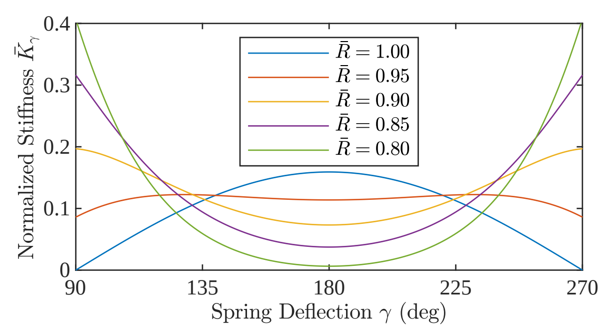

Fig. 4. Normalized (unitless) stiffness versus deflection angle for different values of $\bar{R}$ with $\varphi_A = 180°$ and $\varphi_B = 0°$.

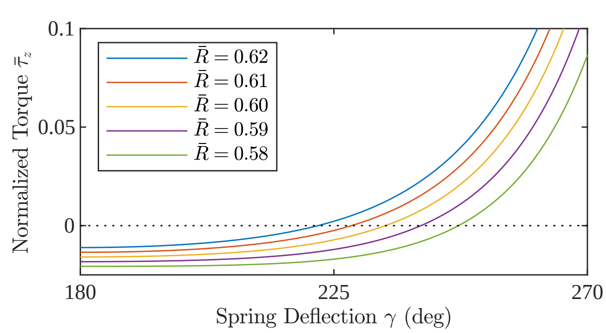

Fig. 5. Normalized (unitless) torque versus deflection angle for different values of $\bar{R}$ with $\varphi_A = 180°$ and $\varphi_B = 90°$.

photograph of the robot with arrows indicating the magnetization directions of the integrated magnets (magnetized by the manufacturer) is shown in Fig. 1(a) and the CAD model of the robot is shown in Fig. 1(b).

Like any design process, designing magnetic torsion springs is an iterative process that may require returning to earlier steps after analyzing the design. The choice of magnetic moment magnitudes was limited by the selection available from magnet parts suppliers, and the distance $r_A + r_B$ was subject to the manufacturing capabilities of the FormLabs Form 2 printer. In order to accommodate the gripping surface of the finger, magnet 2 had to be offset from the center of the gripper by approximately 0.8 mm, which is why the final design of the finger joint had $\varphi_B = 80.5°$.

IV. SMART Spring Model Validation

It was necessary to verify the behavior of the SMART springs, which may differ from the analytical model due to the limitations of the dipole assumption. To accomplish this validation, a magnetic finite element analysis was performed in COMSOL, and experimental measurements of the restoring torque on a scale model of the finger and wrist springs were conducted. The FEA results and experimental measurements are shown in Fig. 8.

A. Finite Element Analysis

A finite element (FE) analysis was performed in COMSOL to ensure that the SMART springs behaved similarly to their analytical approximation. Each SMART spring was simulated individually. The FE model takes the geometry of the magnets into account, so it should show if the dipole assumption made in the analytical model fails to accurately capture the behaviour of the springs. In the simulation for the wrist spring, the base magnet (magnet 0) was held fixed while the wrist magnet (magnet 1) was rotated about the center of rotation in increments of 2° over the operating deflection range ($90° \leq \gamma \leq 270°$ or equivalently $-90° \leq \theta_1 \leq 90°$). Similarly, for the finger spring the wrist magnet (magnet 1) was held fixed while the finger magnet (magnet 2) was rotated about the center of rotation in increments of 2° over the operating deflection range ($189.5° \leq \gamma \leq 279.5°$ or equivalently $0° \leq \theta_2 \leq 90°$). Fig. 6 shows an example position of the finger spring in the FE model.

TABLE I

Summary of the selected design parameters.

Parameter	Wrist Joint	Finger Joint
β	**-180.0°**	**-189.5°**
φ_A (deg)	180.0°	**180.0°**
φ_B (deg)	**0.0°**	**80.5°**
$\bar{R}$ (–)	0.94	0.59
r_A (mm)	0.254	3.302
r_B (mm)	3.969	4.849
m_A (mA·m^2)	3.7	29.6
m_B (mA·m^2)	29.6	12.6

B. Experimental Validation

The spring torque was measured using an ATI Nano17 Titanium 6-axis force-torque transducer with signals acquired through a National Instruments USB-6210 DAQ. The experimental apparatus is pictured in Fig. 7. The torque measurement on link B was performed in a kinematic inversion: link B (the moving link in the model) was held fixed to the force transducer while link A (the fixed link in the model) was rotated around the center of rotation in increments of 5° through the operating deflection range of each spring. There was no physical contact between the links to ensure that the only measured forces were due to magnetic interaction and not friction or contact forces.

The experiments were performed at 200% scale compared to the true robot scale to ensure that the magnetic torques were sufficiently large to be measured by the ATI Nano17T. Consequently, the measured torques in Fig. 8 were scaled by a factor of $1/8$ to account for the scaling of $\tau_z \propto L^3$. For the wrist spring, a D22-N52 magnet and a D44-N52 magnet from K&J magnetics were used for $\boldsymbol{m}_0$ and $\boldsymbol{m}_1$ at distances of $r_A = 0.51$ mm and $r_B = 7.94$ mm respectively. For the finger spring, a D44-N52 magnet and three B222G-N52 magnet from K&J Magnetics were used for $\boldsymbol{m}_1$ and $\boldsymbol{m}_2$ at distances of $r_A = 6.60$ mm and $r_B = 9.70$ mm respectively. The experimental results are shown in Fig. 8(a) and (b) for the wrist spring and finger spring respectively.

The unstable equilibrium point of the finger in the fabricated robot was measured as $\theta_2 = 47° \pm 5°$ by slowly

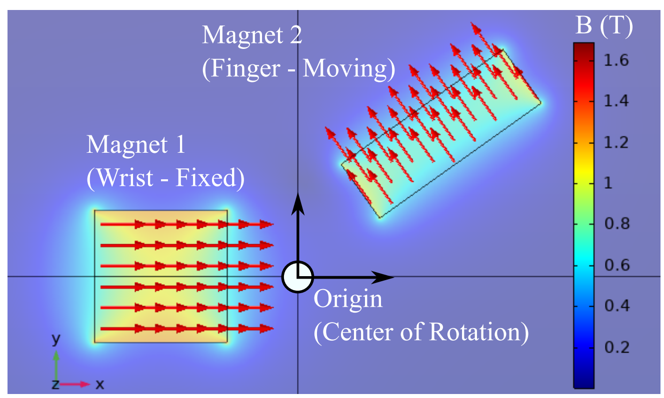

Fig. 6. Example COMSOL simulation. The color bar indicates the magnetic flux density B produced by both magnets at different x-y positions.

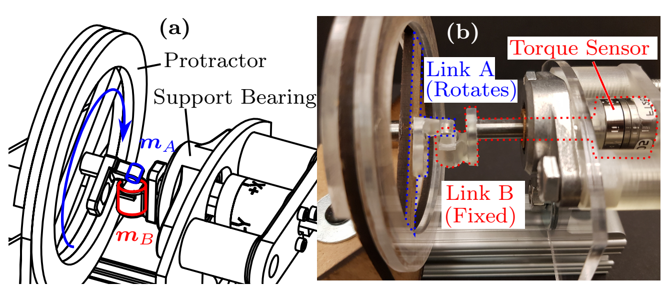

Fig. 7. Experimental apparatus for measuring the torque produced by the SMART spring on link B. **(a)** CAD model, **(b)** photograph.

displacing the finger manually until it snapped to its other stable position. Similarly the stable equilibrium point of the wrist was measured as $\theta_1 = 0° \pm 5°$. Static friction prevented more precise measurements of the equilibrium points.

Finally, the robot was placed inside of a 3-axis Helmholtz coil system capable of producing 20 mT fields in three dimensions at speeds up to 50 Hz. An open-loop control algorithm was used to demonstrate the independent wrist and gripper operation (see the included video). The bistable behavior of the gripper was evident: the gripper would "snap" between its open and closed positions, and it would remain stable in each position even in the absence of opening/closing applied fields. The constant stiffness behavior of the wrist was also observed: linearly increasing field strengths produced linearly increasing joint angles.

V. Discussion

The results in Fig. 8(a) show excellent agreement between the analytical model and the FEA model in predicting the wrist spring torque. The experimental results show reasonable agreement in that the torque is very nearly linear, but the linear best-fit stiffness for the experimental results is 25% lower than the stiffness predicted by the analytical and FEA models. It is possible that tolerances in the construction of the experimental apparatus resulted in a slightly larger spacing between the magnets than intended. Due to the cubic effect of distance $r_A + r_B$ on the stiffness, a misalignment of only 0.5 mm could account for the 25% change in stiffness.

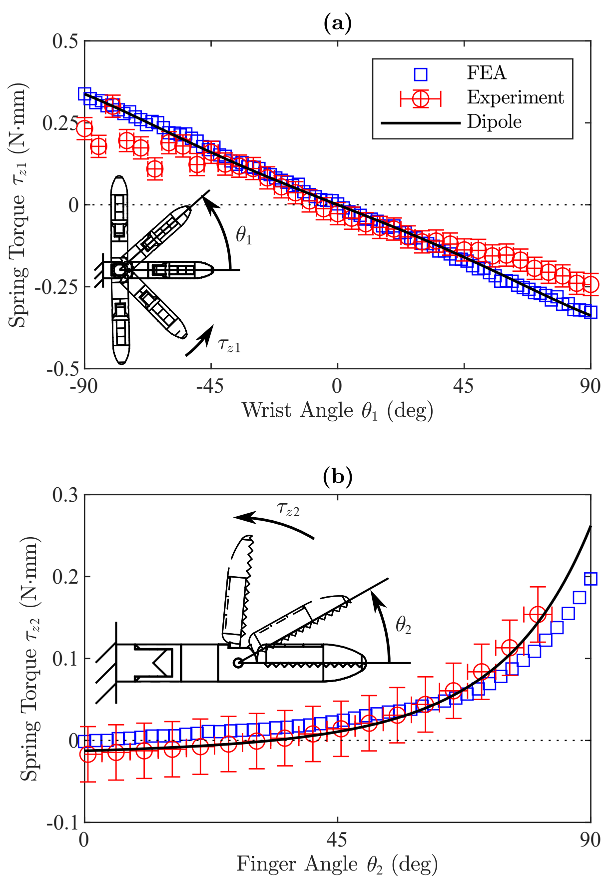

Fig. 8. Predicted dipole model, FEA numerical model, and scaled experimental measured joint torque versus joint angle for **(a)** Wrist joint (constant stiffness) and **(b)** Finger joint (bistable negative stiffness).

The results in Fig. 8(b) show reasonable agreement between the analytical model and the FEA model in predicting the finger spring torque for large values of θ_2 (when the magnets are close together) but slightly worse agreement for small values of θ_2 (when the magnets are farther apart). The worse agreement may be due to the relatively small torques being affected by the numerical precision of the FEA simulation. Conversely, the experimental results show excellent agreement with the analytical model, though the FEA model is well within the range of uncertainty of the experimental measurements. The close agreement between experimental results and theory was unexpected because magnets with higher aspect ratios (like the finger magnet) tend to be poorly represented by the dipole assumption [16].

Overall, the qualitative behaviour of the magnetic robot as it was actuated in a magnetic field was indicative of a successful design. The finger joint exhibited bistability with an unstable equilibrium within the designed region, and the wrist joint responded linearly to increasing torques, which implies a constant-torque wrist spring response. However, static friction in the joint proved to be significant enough to result in steady-state errors in response to step inputs.

A. Limitations and Future Work

Friction in the mechanism was non-negligible. The mechanism components were composed of UV resin and were manufactured with relatively poor tolerances (± 25 μm) compared to other machining processes. A future design could take advantage of precision machining of metal or other low friction materials. Feedback control may also allow some compensation for friction in the future.

The design methodology described here was ad hoc for the specific manipulator geometry. Whether a generalized method for designing or even optimizing SMART springs could be produced remains an open question. Furthermore, the magnetic actuation design of the robot was based on an existing magnetic gripper, but in the future it may be more effective to simultaneously design the SMART spring and magnetic actuation of the robot.

This study was limited to examining the interactions between magnets on adjacent links. However, there are also magnetic interactions between all magnets in the mechanism. Modeling multiple-magnet interactions over the workspace of a serial manipulator and determining their effects on the magnetic spring torques is an area of future work.

While constant stiffness and nonlinear bistable SMART spring were presented here, the design space of SMART springs is vast and highly variable. Other beneficial torque-displacement relationships could produce complex passive behaviours in magnetic mechanisms. For example, it may be possible to manufacture magnetic mechanisms with pop-up behaviours. This paper only scratches the surface of the potential applications of magnetic torsion springs.

References

[1] X.-Z. Chen, B. Jang, D. Ahmed, C. Hu, C. De Marco, M. Hoop, F. Mushtaq, B. J. Nelson, and S. Pané, "Small-Scale Machines Driven by External Power Sources," *Advanced Materials*, vol. 30, pp. 1 705 061(1–22), Feb. 2018.

[2] F. Leong, N. Garbin, C. D. Natali, A. Mohammadi, D. Thiruchelvam, D. Oetomo, and P. Valdastri, "Magnetic surgical instruments for robotic abdominal surgery," *IEEE Reviews in Biomedical Engineering*, vol. 9, pp. 66–78, 2016.

[3] J. Chen, Z. Liang, Y. Zhu, C. Liu, L. Zhang, L. Hao, and J. Zhao, "Towards the exploitation of physical compliance in segmented and electrically actuated robotic legs: A review focused on elastic mechanisms," *Sensors*, vol. 19, pp. 5351(1–22), Dec. 2019.

[4] M. A. Woodward and M. Sitti, "Universal Custom Complex Magnetic Spring Design Methodology," *IEEE Transactions on Magnetics*, vol. 54, no. 1, p. 8200213, Jan. 2018.

[5] ——, "Tailored Magnetic Springs for Shape-Memory Alloy Actuated Mechanisms in Miniature Robots," *IEEE Transactions on Robotics*, vol. 35, no. 3, pp. 589–601, June 2019.

[6] J. Choi, S. Park, W. Lee, and S.-C. Kang, "Design of a robot joint with variable stiffness," in *IEEE International Conference on Robotics and Automation (ICRA)*, Pasadena, USA, May 2008, pp. 1760–1765.

[7] A. Sudano, D. Accoto, L. Zollo, and E. Guglielmelli, "Design, development and scaling analysis of a variable stiffness magnetic torsion spring," *International Journal of Advanced Robotic Systems*, vol. 10, pp. 372:2013(1–11), 2013.

[8] A. Sudano, N. L. Tagliamonte, D. Accoto, and E. Guglielmelli, "A resonant parallel elastic actuator for biorobotic applications," in *IEEE/RSJ International Conference on Intelligent Robots and Systems (IROS)*, Chicago, USA, Sept. 2014, pp. 2815–2820.

[9] Y. Zheng, X. Zhang, Y. Luo, Y. Zhang, and S. Xie, "Analytical study of a quasi-zero stiffness coupling using a torsion magnetic spring with negative stiffness," *Mechanical Systems and Signal Processing*, vol. 100, pp. 135–151, Feb. 2018.

[10] M. C. Hoang, V. H. Le, J. Kim, E. Choi, B. Kang, J.-O. Park, and C.-S. Kim, "Untethered Robotic Motion and Rotating Blade Mechanism for Actively Locomotive Biopsy Capsule Endoscope," *IEEE Access*, vol. 7, pp. 93 364–93 374, July 2019.

[11] M. Simi, G. Gerboni, A. Menciassi, and P. Valdastri, "Magnetic Torsion Spring Mechanism for a Wireless Biopsy Capsule," *Journal of Medical Devices*, vol. 7, no. 4, p. 041009, Dec. 2013.

[12] C. Forbrigger, A. Lim, O. Onaizah, S. Salmanipour, T. Looi, J. M. Drake, and E. Diller, "Cable-less, Magnetically-Driven Forceps For Minimally Invasive Surgery," *IEEE Robotics and Automation Letters*, vol. 4, no. 2, pp. 1202–1207, apr 2019.

[13] A. Lim, A. Schonewille, C. Forbrigger, T. Looi, J. M. Drake, and E. Diller, "Design and Comparison of Magnetically-Actuated Dexterous Forceps Instruments for Neuroendoscopy," *IEEE Transactions on Biomedical Engineering*, vol. 68, no. 3, pp. 846–856, Mar. 2021.

[14] L. L. Howell, *Compliant Mechanisms*. John Wiley & Sons, Inc., 2001.

[15] J. J. Abbott, E. Diller, and A. J. Petruska, "Magnetic Methods in Robotics," *Annual Review of Control, Robotics, and Autonomous Systems*, vol. 3, pp. 2.1–2.34, 2020. [Online]. Available: doi.org/10.1146/annurev-control-081219-082713

[16] A. J. Petruska and J. J. Abbott, "Optimal permanent-magnet geometries for dipole field approximation," *IEEE Transactions on Magnetics*, vol. 49, no. 2, pp. 811–819, Feb. 2013.